Journal of Materials Chemistry A

ROYAL SOCIETY OF CHEMISTRY

PAPER

View Article Online
View Journal | View Issue

Cite this: J. Mater. Chem. A, 2024, 12, 11691

Bio-inspired design of a self-supported bismuth microforest for high performance sodium storage†

Jia Bai,[a] Yan Liu,*[a] Ben Pu,[a] Qi Tang,[a] Yongbin Wang,[a] Ruihan Yuan,[b] Jin Cui,[a] Yi Yang,[a] Xiaojia Zheng,[b] Bin Zhou *[b] and Weiqing Yang *[ac]

Received 9th February 2024
Accepted 10th April 2024

DOI: 10.1039/d4ta00950a

rsc.li/materials-a

The sodium-ion battery (SIB) as a promising candidate for large-scale energy storage has attracted widespread attention in recent years. However, its practical application is plagued by the lack of suitable anode materials that can afford long cycle life, high rate capability and large capacity. Herein, we report a high-performance self-supported Bi microforest (MF) anode with Bi microtree arrays uniformly grown on porous Cu foil for SIBs. The Bi MF can be directly employed as an anode without using any binders and conductive additives. Finite-element analysis and electrochemical kinetics analyses reveal that such a tree-like microstructure facilitates fast Na^+ diffusion and promotes effective stress dissipation. As a result, the Bi MF electrode shows exceptionally high rate capability (338.9 mA h g^{-1} at 50 A g^{-1} with a capacity retention of 94.2%) and excellent cycling stability (95.9% capacity retention after 1200 cycles at 1 A g^{-1}). More importantly, by pairing the Bi MF anode with a $Na_3V_2(PO_4)_3$ cathode, the assembled full cell achieves a long cycle life and an inspiring energy density of 132.2 W h kg^{-1}, showing the great potential of the Bi MF anode in sodium-ion full-cells.

Introduction

The increasing demand for large-scale electrical energy storage systems necessitates the development of low-cost, environmentally benign and safe energy storage technologies.[1–4] Sodium-ion batteries (SIBs) perfectly fulfill these requirements and thus have drawn worldwide interest from both academia and industry.[5–9] One of the major scientific challenges for the development of SIB technology is the lack of high performance anode materials.[10–12] To date, various materials such as carbonaceous materials,[13–15] metal chalcogenides,[16–21] and alloy-type materials (*e.g.*, P,[22–25] Sb,[26–28] Bi,[29–31] Sn[32–36]) have been extensively investigated as the anode materials for SIBs. Among these candidates, Bi is regarded as one of the most promising anodes because of its high theoretical capacity (385 mA h g^{-1} for gravimetric capacity and 3765 mA h cm^{-3} for volumetric capacity), suitable reaction potential (~0.6 V *vs.* Na^+/Na) and special buckled-layer crystal structure with a large interlayer spacing, which allows for fast Na^+ insertion/extraction.[37–42] However, the dramatic volume change (~250%) during the sodiation/desodiation process is a critical barrier for the practical application of Bi-based anodes.[43,44] Such a volume variation causes electrode pulverization and continuous solid-electrolyte interphase (SEI) breaking/reformation during repeated cycling, resulting in poor cycle life and rate capability.[45]

To address the aforementioned issues, tremendous efforts have been made toward improving the cycling performance of Bi-based anodes, such as designing micro/nanostructures (*e.g.*, Bi nanotubes,[46] few-layer bismuthene,[47–50] Bi nanoflakes[51]), forming alloys with inactive/active metals (*e.g.*, Bi–Sb,[52,53] Bi–Sn,[54] Bi–Ni[55,56]), encapsulating Bi in carbon matrixes (*e.g.*, Bi nanoparticle@C composites,[57–60] yolk/core–shell Bi@C nanospheres,[61,62] Bi nanorod@N-doped C nanotubes[63]) and regulating electrolyte composition (*e.g.*, glyme-based electrolytes,[64] tetrahydrofuran-based electrolytes[65,66]). These strategies effectively promote the sodium storage performance of Bi, but improvements are still unsatisfactory. Among various strategies, designing hierarchical micro/nanostructures, especially self-supported three-dimensional architecture, has been proven to be one of the most effective ways for promoting the structural stability and electrochemical performance of alloy-based anode materials. For example, Lei *et al.* fabricated a freestanding Sb nanorod array electrode through electrodeposition with an AAO template and found that such a structural design can ensure efficient electron transport, high ion accessibility, and strong structural integrity, thus showing excellent cycling stability and rate capability.[67] Li *et al.* designed a self-supported Sb prism and $Bi_{0.75}Sb_{0.25}$ pyramid arrays on Cu substrates *via* template-free electrodeposition methods and observed a robust rate

[a]Key Laboratory of Advanced Technologies of Materials (Ministry of Education), School of Materials Science and Engineering, Southwest Jiaotong University, Chengdu, 610031, PR China. E-mail: y_liu@swjtu.edu.cn; wqyang@swjtu.edu.cn

[b]Sichuan Research Center of New Materials, Institute of Chemical Materials, China Academy of Engineering Physics, Chengdu, 610200, PR China. E-mail: bzhou@caep.cn

[c]Research Institute of Frontier Science, Southwest Jiaotong University, Chengdu, 610031, PR China

† Electronic supplementary information (ESI) available. See DOI: https://doi.org/10.1039/d4ta00950a

capability and cycling stability toward sodium storage.[68,69] Similarly, Yu *et al.* prepared SbSn pyramid arrays on Cu substrates *via* electrodeposition and demonstrated that the pyramid-like structure is conducive to Na^+ diffusion and stress dissipation.[70] Considering that Bi confronts the same volume expansion issues and shares the similar sodium storage mechanism with the other alloy-type materials, the above strategy should also be valid for Bi. Therefore, it is highly desirable to explore the sodium storage performance of self-supported three-dimensional Bi anodes.

Natural systems offer many ingenious prototypes for the discovery of innovative material designs with broad applications.[71,72] It is well known that trees play an important role in natural ecosystems, as their leaves efficiently harvest sunlight and quickly capture/release gases, while their branches and trunks facilitate the fast transportation of nutrient substances.[73] Herein, inspired by the natural tree structure, we design and develop a self-supported Bi microforest (MF) anode with Bi microtree arrays uniformly grown on porous Cu foil *via* a simple, efficient and scalable *in situ* galvanic replacement approach for SIBs. Such a structure offers several key advantages for electrochemical sodium storage: (i) the hierarchical tree-like micro–nanostructure creates a large contact area with the electrolyte and a small difference in the Na^+ concentration gradient, thus improving Na^+ accessibility and facilitating fast Na^+ diffusion; (ii) the sufficient spacing between Bi microtrees offers sufficient room to accommodate the volume expansion of Bi during cycling; (iii) the Bi microtrees are directly grown on copper foil, enabling fast electron transport. Moreover, the Bi MF electrode can be directly employed as an anode for SIBs without any binders and conductive additives, thus minimizing side reactions and endowing the electrode with high initial coulombic efficiency (ICE). As a result, the Bi MF anode exhibits extraordinary rate capability and outstanding cycling stability.

Experimental

Synthesis of Bi MF electrodes

In a typical synthesis, the porous Cu foil discs (12 mm in diameter) were washed sequentially with acetone, 1 M hydrochloric acid, deionized water and ethanol under sonication for 10 min each and then dried under vacuum for 10 h at room temperature. Afterwards, the cleaned porous Cu foil discs were immersed into a solution containing 0.05 M $Bi(NO_3)_3$ and 0.5 M HNO_3 in a mixed solvent of water and acetonitrile (v/v = 1 : 1). The Cu foil immediately underwent a galvanic replacement reaction and its color was changed from red-brown to gray-black. After 3 s, the Cu foil was rinsed with deionized water and ethanol, and dried under vacuum for 10 h.

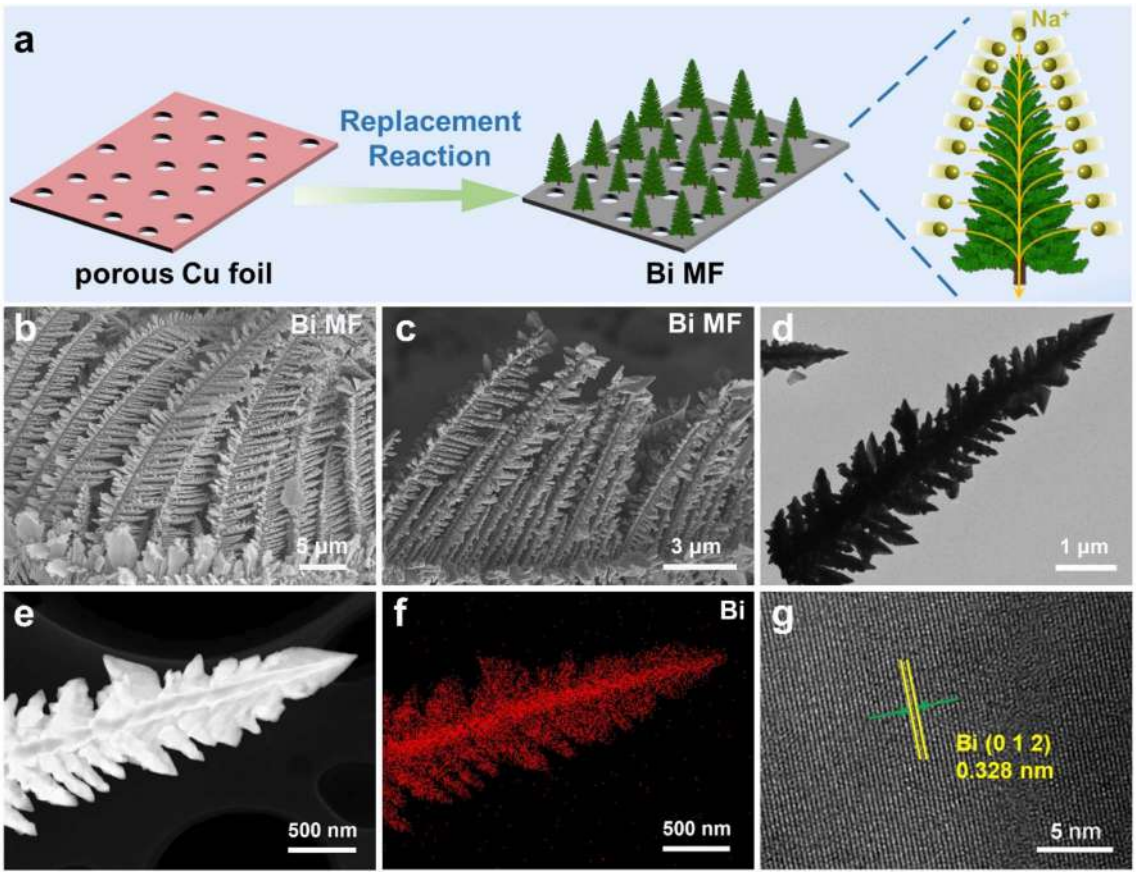

Fig. 1 (a) Schematic illustration of the synthesis of Bi MF. (b and c) SEM images, (d) TEM image, (e and f) elemental mapping, and (g) HRTEM image of Bi MF.

Characterization

The morphology and microstructure of samples were observed by scanning electron microscopy (SEM, JSM-7800 Prime, JEOL), transmission electron microscopy (TEM, HT7700, Hitachi) and high-resolution TEM (HRTEM, Libra 200FE, Zeiss). X-ray diffraction (XRD) patterns were recorded on a PANalytical X'Pert powder diffractometer with Cu Kα radiation. Raman spectra were collected with a Raman spectrometer (Jobin-Yvon XploRA, Horiba) at 532 nm. X-ray photoelectron spectrometry (XPS) spectra were acquired from a Thermo Scientific ESCALAB 250Xi spectrometer.

Electrochemical measurements

The Bi MF discs were directly used as the working electrode. Bulk Bi electrode contained Bi, carbon black and carboxymethyl cellulose at a mass ratio of 8 : 1 : 1. The active material mass loading of Bi-based electrodes was approximately 1 mg cm^{-2}. Both half-cells and $Na_3V_2(PO_4)_3$ (NVP)||Bi MF full cells were assembled in an Ar-filled glove box. In the half-cell, the working electrode was the Bi MF, while sodium foil acted as the counter electrode. For the full cell, the anode was the Bi MF electrode, and the cathode was the NVP electrode. The NVP electrode was prepared by coating a slurry containing 92% NVP, 4% carbon black and 4% polyvinylidene difluoride onto aluminum foil. The mass loading of $Na_3V_2(PO_4)_3$ in the cathode was approximately 4.5 mg cm^{-2}. The mass ratio of the cathode to anode was approximately 4.5 : 1. The separator was a glass fiber (Whatman GF/D) and the electrolyte was 1 M $NaPF_6$ in DME. Galvanostatic charge–discharge tests were measured using a Neware battery measurement system. Rate performance was evaluated using an Arbin MSTAT4 testing system. Electrochemical impedance spectroscopy (EIS) and cyclic voltammetry (CV) tests were carried out on an Admiral Squidstat Prime electrochemical workstation. The galvanostatic intermittent titration technique (GITT) was conducted with a LAND CT3001A battery testing system.

Results & discussion

The Bi MF electrodes were prepared by a facile acetonitrile-assisted galvanic replacement method[74] as shown in Fig. 1a. After the porous copper foil was immersed in a bismuth salt aqueous solution containing acetonitrile, galvanic replacement took place immediately at the surface of the copper foil, evidenced by the simultaneous color change of the copper foil from reddish to black (Fig. S1, ESI†). SEM and TEM images reveal that many microtrees grow on the surface of the porous copper foil, forming a microforest (Fig. 1b–d, S2, and S3, ESI†). The formation of microtrees is probably associated with the fast reaction kinetics of the galvanic replacement reaction, which creates diffusion-limited nonequilibrium conditions and thus promotes

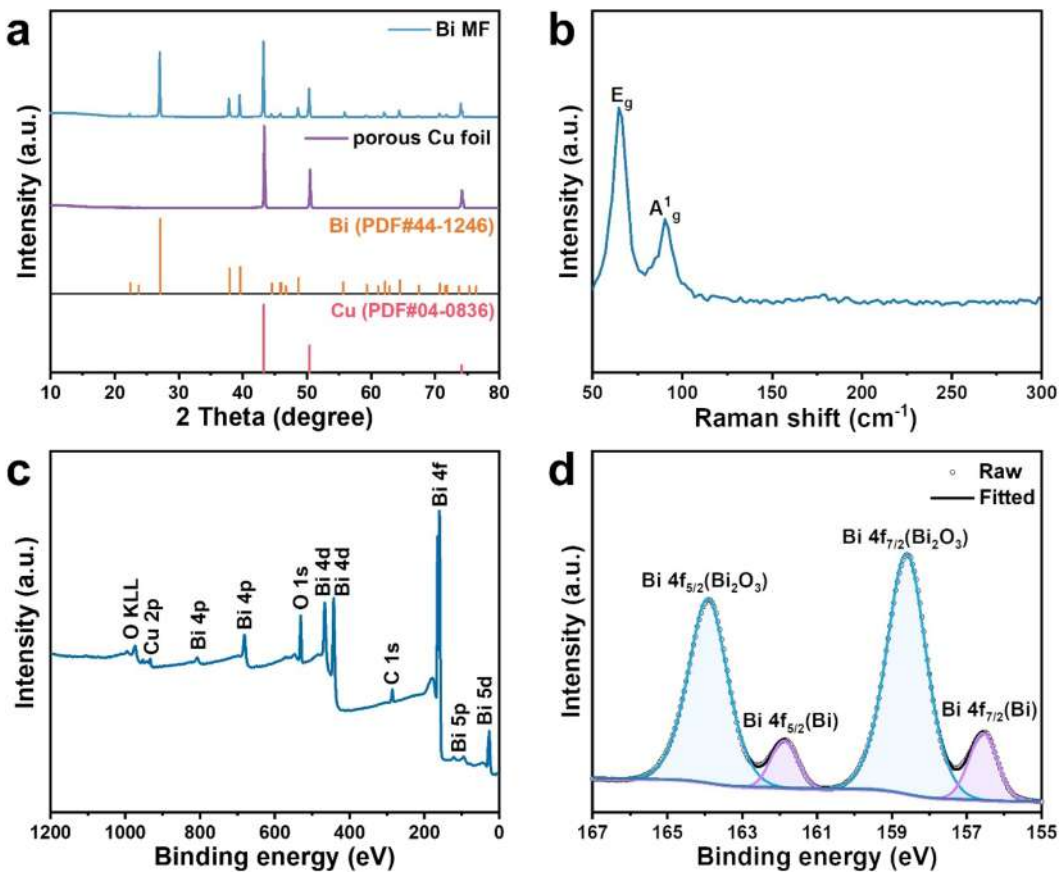

Fig. 2 (a) XRD patterns of Bi MF and porous Cu foil. (b) Raman spectra, (c) XPS survey spectrum, (d) high-resolution Bi 4f spectrum of Bi MF.

the growth of Bi protrusions formed at the initial stage of the replacement reaction, resulting in the growth of Bi microtrees (Fig. S4†).[75–77] The energy dispersive X-ray spectroscopy (EDS) elemental mapping (Fig. 1e and f) and HRTEM images (Fig. 1g) indicate that these microtrees consist of metallic Bi. The formation of Bi microtrees was further confirmed by XRD, Raman spectroscopy and XPS measurements.

As shown in Fig. 2a, all diffraction peaks in the XRD pattern of the Bi MF can match nicely with the rhombohedral Bi (PDF#44-1246) and face-centered cubic Cu (PDF#04-0836), indicating that no additional impurities are introduced during the generation of Bi microtrees. According to the Scherrer equation ($D = k\lambda/\beta \cos\theta$), the average crystallite size of the bismuth microforest is approximately 44.4 nm.[78–80] The Raman spectra display two peaks at 64.9 and 90.6 cm^{-1} (Fig. 2b), which can be assigned to the in-plane E_g and the out-plane A_g^1 vibrational modes of metallic Bi, respectively.[46] XPS was used to investigate the surface characteristics of the Bi MF. The survey spectrum (Fig. 2c) reveals that the surface of Bi MF mainly consists of Bi element. The high-resolution Bi 4f XPS spectrum (Fig. 2d) exhibits two sets of doublets (Bi $4f_{5/2}$ and Bi $4f_{7/2}$). The low-intensity doublets located at 161.9 and 156.6 eV can be assigned to metallic Bi, while the high-intensity doublets presented at 163.9 and 158.6 eV can be ascribed to Bi_2O_3.[41,81] The presence of Bi_2O_3 on the surface of the Bi MF is owing to surface oxidation, which is a common phenomenon for metallic Bi. Combining with the XRD and Raman results which revealed that no Bi_2O_3 signal is detected, it can be inferred that the oxidation is limited to the surface of Bi MF and the content of Bi_2O_3 is negligible.

To demonstrate the potentiality of Bi MF in SIBs, we assessed its sodium storage performance in coin-type half-cells. The CV

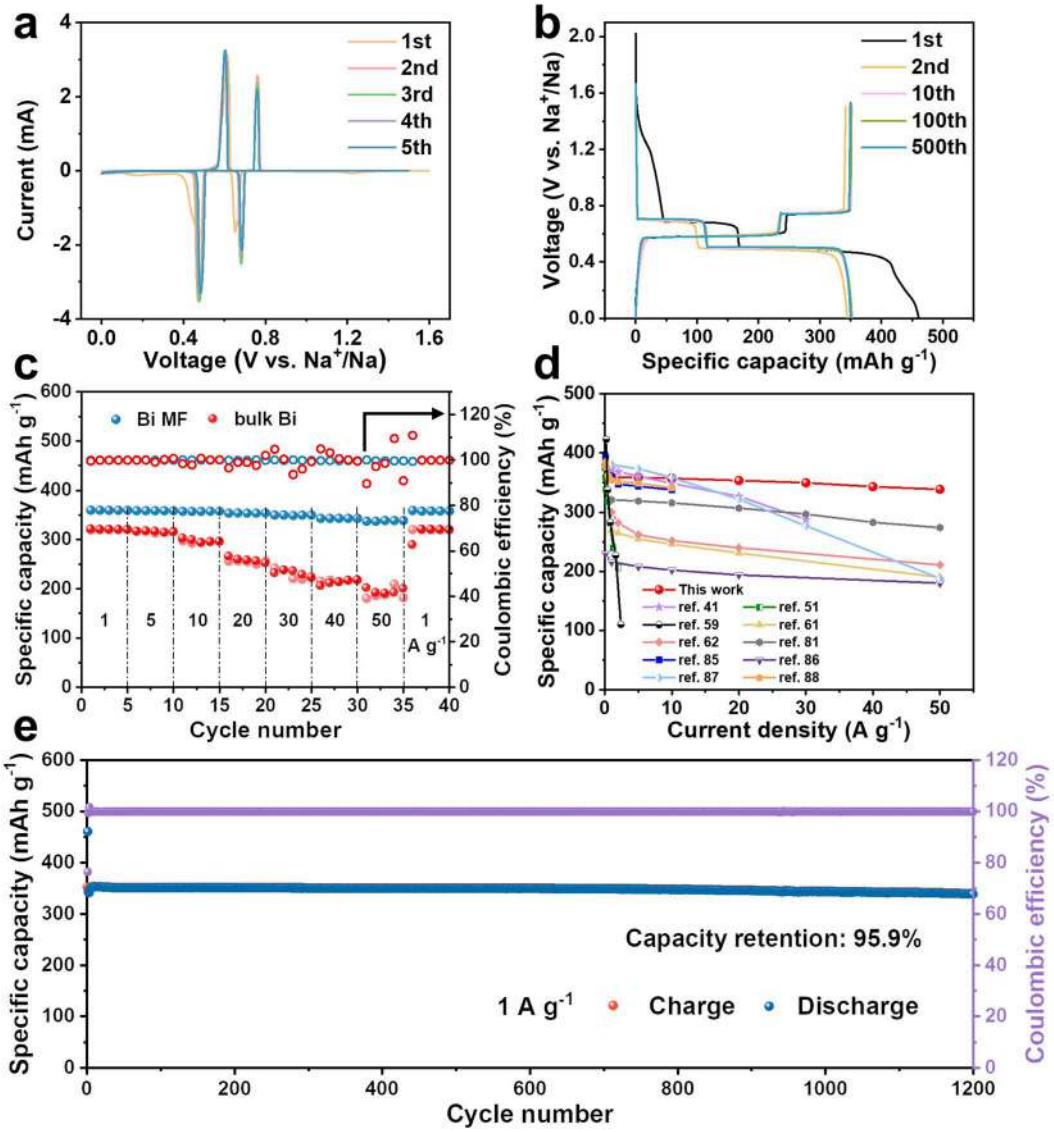

Fig. 3 (a) CV curves of the Bi MF electrode at 0.1 mV s^{-1}. (b) GCD curves of the Bi MF electrode at 1 A g^{-1}. (c) Comparison of the rate capability of the Bi MF and bulk Bi electrodes. (d) Comparison of the rate capability of the Bi MF and many previously reported Bi-based anodes for SIBs. (e) Long-term cycling performance of the Bi MF electrode at 1 A g^{-1}.

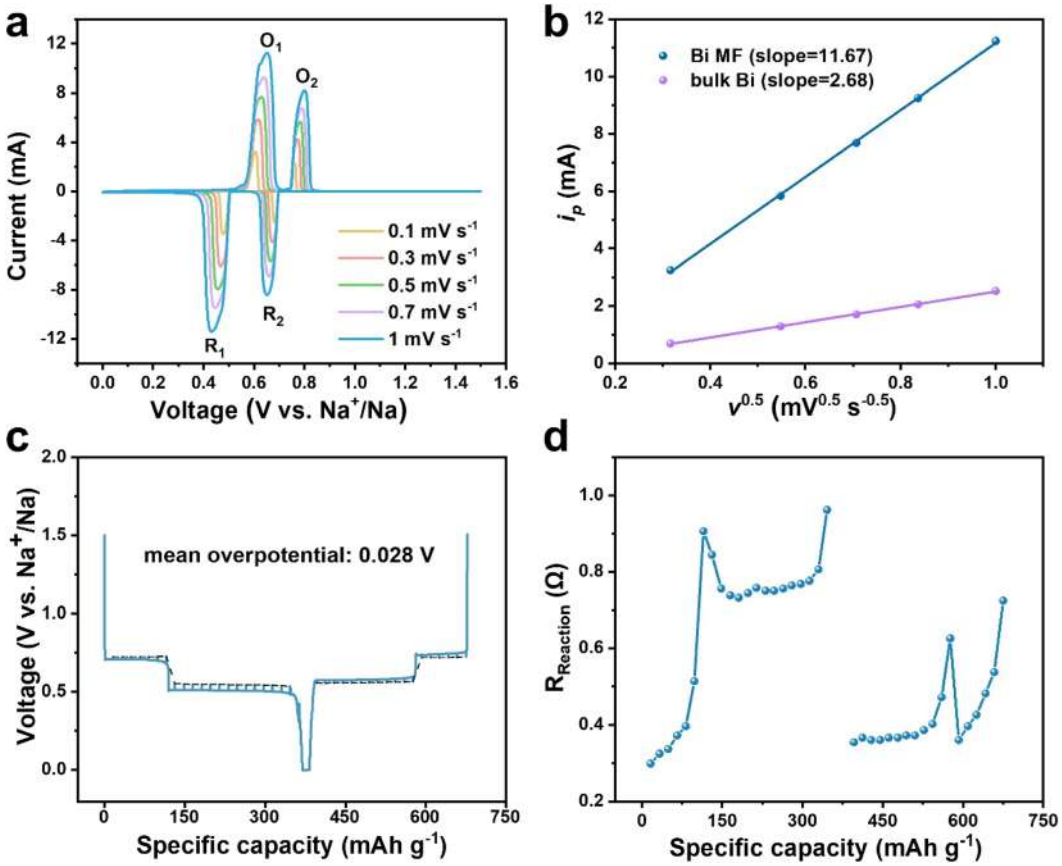

Fig. 4 (a) CV curves of the Bi MF electrode at varying scan rates. (b) Linear fitting for the peak current *versus* (scan rate)$^{0.5}$ plots of the Bi MF and bulk Bi electrodes. (c) Potential response and quasi-equilibrium open-circuit voltages (dotted lines) of the Bi MF electrode during GITT measurement. (d) The reaction resistance of the Bi MF electrode.

curves of the Bi MF electrode over the first 5 cycles were acquired at a scan rate of 0.1 mV s^{-1} in the voltage range of 0.01 to 1.5 V (Fig. 3a). Two broad weak peaks located at 1.22 and 0.17 V in the first cathodic scan, which subsequently vanish in the following cycles, are associated with some irreversible processes, such as the formation of the SEI layer.[46,82] The two cathodic peaks at 0.65 and 0.47 V reflect the stepwise alloying process of Bi → NaBi → Na_3Bi, while the two anodic peaks at 0.62 and 0.76 V represent the stepwise dealloying process of Na_3Bi → NaBi → Bi.[83,84] The CV curves of the Bi MF almost overlap after the first CV cycle, indicating superior electrochemical reversibility of the Bi MF electrodes. As shown in Fig. 3b, the galvanostatic charge–discharge (GCD) curves at the current density of 1 A g^{-1} depict two obvious voltage plateaus well matching the redox peaks in the CV curves. The Bi MF delivers an initial discharge capacity of 460.4 mA h g^{-1} with an ICE of 76.5%. The relatively high ICE can be attributed to the self-supporting electrode design which avoids the use of additives (*e.g.*, conductive agents and binders) and the good compatibility between Bi and ether electrolyte.

The Bi MF electrode exhibits extraordinary rate capability. As shown in Fig. 3c and S5 (ESI),† the Bi MF electrode delivers reversible capacities of 359.7, 358.9, 357.5, 353.9, 350.0, 343.4 and 338.9 mA h g^{-1}, at current densities of 1, 5, 10, 20, 30, 40 and 50 A g^{-1}, respectively, suggesting that an extremely high capacity retention of 94.2% is achieved with the current density dramatically increased by 50 times. In comparison, the bulk bismuth electrode shows a fast capacity decaywith increasing current density and only exhibits a low capacity retention of 59.4%. The excellent rate performance of the Bi MF electrode outperforms that of most Bi-based anodes reported to date (Fig. 3d and Table S1, ESI†) and can be attributed to the hierarchical tree-like microstructure of Bi MF, which allows for fast Na^+ diffusion and efficient charge transport.[41,51,59,61,62,81,85–88] To investigate the influence of pores in the copper foil on the electrode performance, the rate performance of Bi MF grown on porous and non-porous copper foil are compared in Fig. S6 and S7, ESI.† The Bi MF electrode prepared on the porous copper foil exhibits better rate capability than that prepared on the non-porous copper foil, suggesting that the pores on the copper foil also facilitate fast Na^+ diffusion. Moreover, to assess the effect of mass loading on the electrochemical performance of the electrodes, Bi MF electrodes with different mass loadings were prepared *via* adjusting the reaction time of the replacement reaction. As shown in Fig. S8, ESI,† the rate capability of the Bi MF electrode decreases with increasing bismuth loading, particularly under high-rate conditions, which might be attributed to the sluggish Na^+ diffusion in thick films.

Additionally, the Bi MF electrode also exhibits superior cycling stability. As demonstrated in Fig. 3e, it can still maintain a high reversible capacity of 338.6 mA h g^{-1} with almost no capacity loss even after 1200 cycles at 1 A g^{-1}, corresponding to a capacity retention of 95.9%.

In order to investigate the reasons for the superior electrochemical performance of the Bi MF electrodes, a range of electrochemical tests were performed. Fig. 4a shows the CV curves acquired at different scan rates from 0.1 to 1.0 mV s^{-1}. The relationship between the peak current (i_p, mA) and the scan rate (v, mV s^{-1}) obeys the following Randles–Sevcik equation:

$$i_p = 2.69 \times 10^5 A C_{Na^+} n^{3/2} D_{Na^+}^{1/2} v^{1/2}$$

where A is the area of the electrode, C_{Na^+} is the concentration of Na^+, and n is the charge-transfer number.[89] Accordingly, the Na^+ diffusion coefficients (D_{Na^+}) of the Bi MF electrode is calculated to be 5.45 $\times$ 10^{-11} cm^2 s^{-1}, which is at least an order of magnitude higher than that of bulk Bi (2.87 $\times$ 10^{-12} cm^2 s^{-1}) (Fig. 4b and S9, ESI†), suggesting that the tree-like structure is more favorable for fast Na^+ diffusion. The GITT was adopted to study the kinetics of Na^+ storage behavior. Fig. 4c depicts the potential responses and equilibrium open-circuit voltages (dotted lines) of the Bi MF electrode during the GITT measurement. Fig. 4d displays the reaction resistances of Bi MF calculated from the GITT curves by dividing the overpotentials by pulse current. As can be seen, the Bi MF shows very low

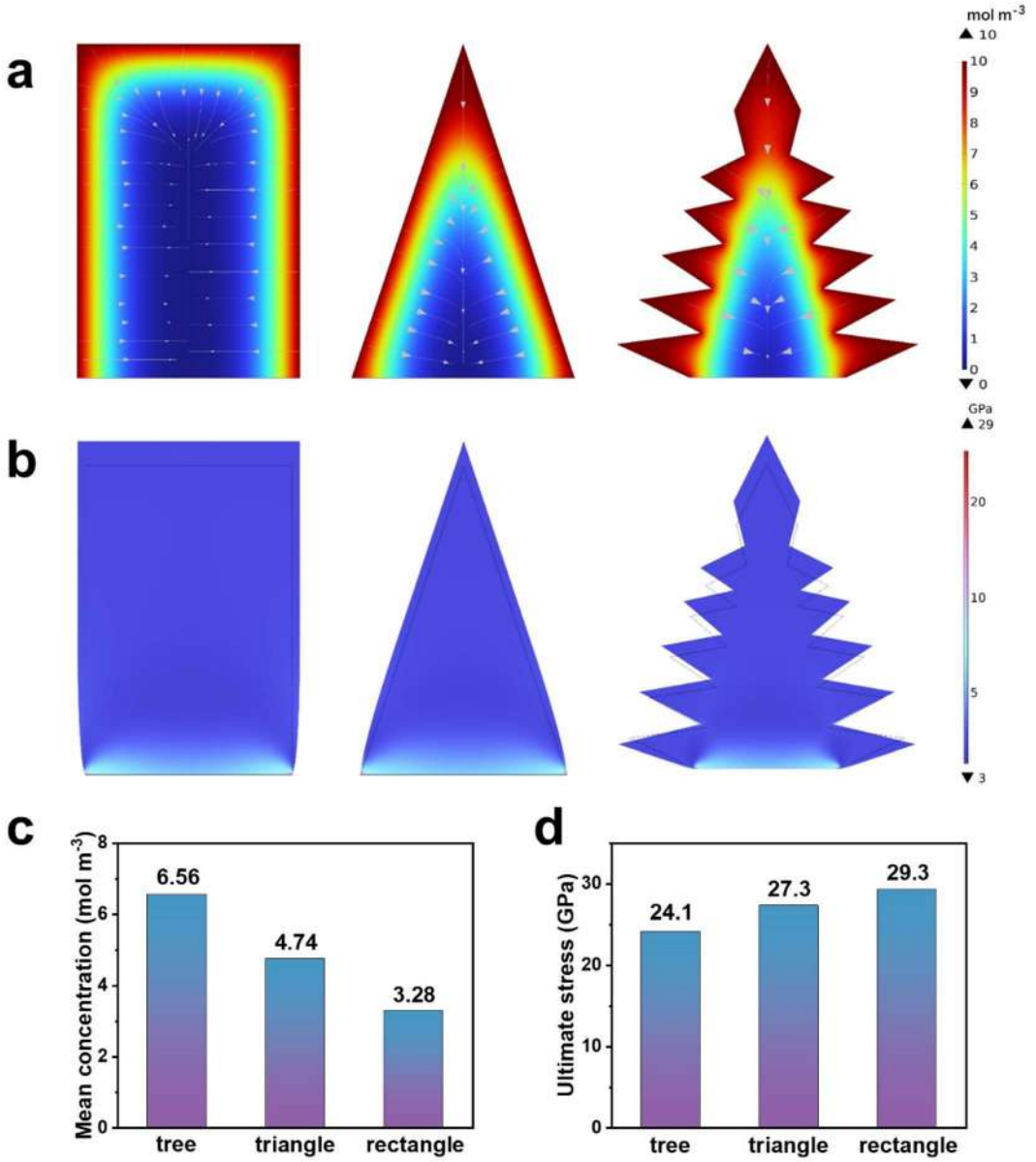

Fig. 5 Finite-element analysis of the distribution of Na^+ concentration and stress in three shapes at the same bottom boundary. (a) Na^+ concentration and (b) stress distributions in these three shapes. The comparison of (c) the mean concentration of Na^+, (d) local maximal stress in these three shapes.

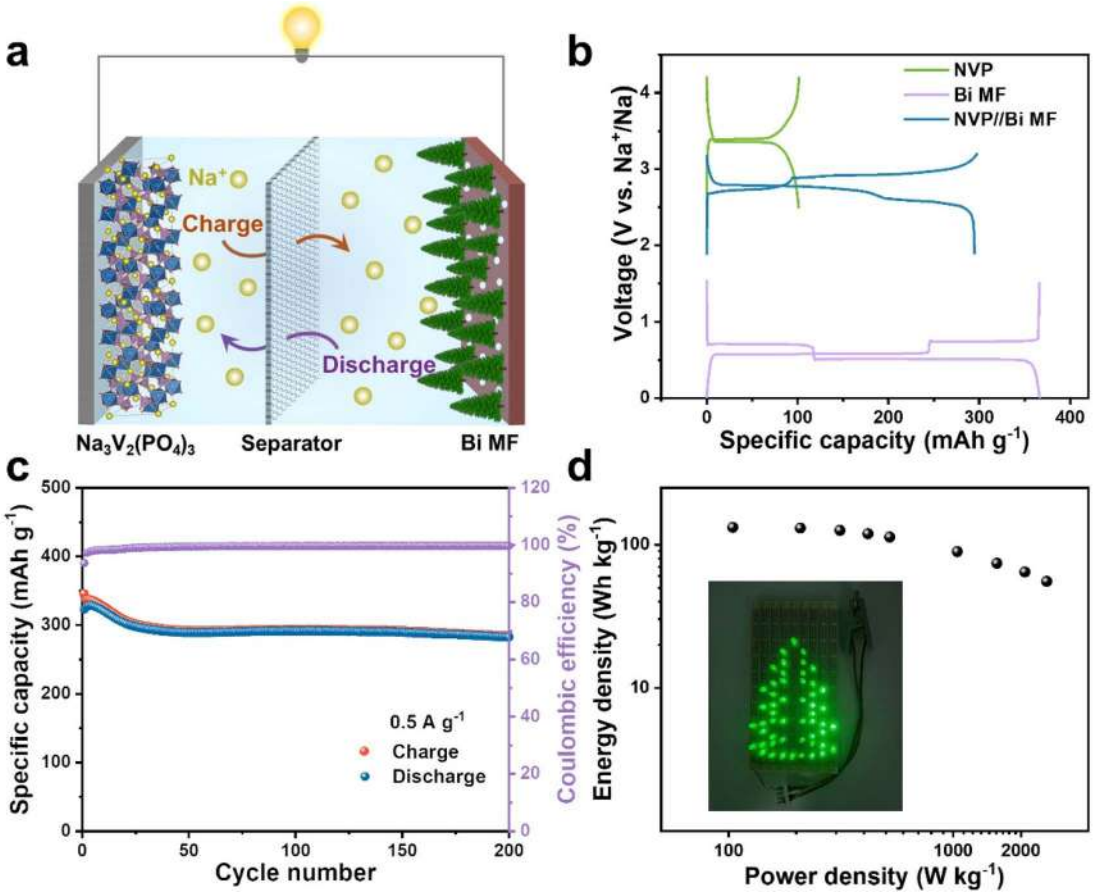

Fig. 6 (a) Schematic showing the NVP||Bi MF full cell. (b) GCD curves of the NVP cathode, Bi MF anode and NVP||Bi MF full cell. (c) Cycling performance of the NVP||Bi MF full cell at 0.5 A g^{-1}. (d) Ragone plot of the NVP||Bi MF full cell (based on the total mass of the anode and cathode). The inset of (d) shows the photograph of a tree-like LED panel lit by an NVP||Bi MF full cell.

overpotentials with an average value of 0.028 V (Fig. 4c) and low reaction resistances (<1 Ω g^{-1}, Fig. 4d) during the charge–discharge process, thus ensuring superior rate performance. The charge transport kinetics of the Bi MF electrode was further investigated by electrochemical impedance spectroscopy (EIS). The Bi MF electrode exhibits lower charge-transfer resistances than the bulk Bi electrode during cycling (Fig. S10, S11 and Tables S2, S3, ESI†), implying that the tree-like structure is conducive to improving the charge transport kinetics.

To reveal the origin of the superior electrochemical performance of the Bi MF electrode, finite element analysis was performed. Three electrochemical models with different geometries, including rectangle, triangle and tree-like shape, were constructed to investigate the effects of geometrical structures on charge transport kinetics and stress distribution. Fig. 5a depicts the 2D contour plots of Na^+ concentration for different geometrical shapes at the initial stage of sodiation. As can be seen, the tree-like shape exhibits the smallest Na^+ depletion zone (deep blue region) among the three shapes. In addition, it also shows the highest average Na^+ concentration (Fig. 5c), implying that the tree-like shape is more beneficial for efficient Na^+ diffusion. It is well known that the high local stress or uneven stress distribution may destroy the integrity of the material. Fig. 5b shows the stress distribution of the three shapes during the sodiation process. In all three shapes, the local stress is mainly concentrated at the bottom of the shapes and the maximal values appear at the bottom corners. Compared to the rectangle and triangle, the tree-like shape shows a more even distribution of stress (Fig. 5b) and much lower maximal local stress (Fig. 5d), thus allowing for more effective stress dissipation.

Encouraged by the excellent electrochemical performance of Bi MF, full cells (Fig. 6a) were assembled by pairing the Bi MF anode with the NVP cathode to assess the feasibility of Bi MF for practical application. The cycling performance of the NVP cathode is shown in Fig. S12, ESI.† As shown in Fig. 6b, the full cell delivers a capacity of 294.7 mA h g^{-1} with a working voltage of approximately 2.6 V at 0.5 A g^{-1} (based on the anode mass). Moreover, the full cell maintains a high capacity of 282.8 mA h g^{-1} after 200 cycles at 0.5 A g^{-1} (Fig. 6c). Additionally, the full cell affords a high energy density of 132.2 W h kg^{-1} at a power density of 104.2 W kg^{-1} (based on the total mass of the anode and cathode, Fig. 6d). The superior full cell performance demonstrates the great promise of the Bi MF electrode for practical application.

Conclusions

In summary, 3D self-supporting Bi MF electrodes with hierarchical micro-nanostructures have been successfully synthesized *via* a facile *in situ* galvanic replacement method, and used as binder- and conductive additive-free anodes for SIBs. The unique microtree structure can promote the accessibility of ions, improve Na^+ diffusion kinetics and facilitate stress dissipation. Thanks to these merits, the Bi MF electrode achieves extraordinary rate performance (maintain 94.2% capacity at 50 A g^{-1}) and outstanding cycling stability (95.9% capacity retention after 1200 cycles at 1 A g^{-1}). Moreover, the full cell with a Bi MF anode also exhibits superior cycling performance. The bio-inspired design strategy will shed light on the future design of high-performance electrodes for SIBs.

Author contributions

J. B., Y. L. and B. Z. conceived and designed the research. J. B., Y. L., B. P. and B. Z. executed the experimental work. J. B., B. P., R. Y., J. C., Y. Y. and X. Z. conducted the characterizations of materials. J. B. and B. P. conducted electrochemical measurements. J. B., Q. T. and Y. W. designed and drew the schematic figures. J. B., Y. L. and B. Z. conducted data analysis. J. B. wrote the original draft. J. B., B. Z. and W. Y. reviewed and edited the manuscript. Y. L., B. Z. and W. Y. supervised the research. All authors discussed the results and approved the final manuscript.

Conflicts of interest

The authors declare no competing financial interests.

Acknowledgements

This work is financially supported by the National Natural Science Foundation of China (Grant No. 52372228), Sichuan Science and Technology Program (Grant No. 2022YFG0293), and Science Foundation of Institute of Chemical Materials (Grant No. SXK-2021-09).

References

1 T. Liu, Y. Zhang, Z. Jiang, X. Zeng, J. Ji, Z. Li, X. Gao, M. Sun, Z. Lin, M. Ling, J. Zheng and C. Liang, *Energy Environ. Sci.*, 2019, **12**, 1512–1533.
2 C. Zhao, Q. Wang, Z. Yao, J. Wang, B. Sánchez-Lengeling, F. Ding, X. Qi, Y. Lu, X. Bai, B. Li, H. Li, A. Aspuru-Guzik, X. Huang, C. Delmas, M. Wagemaker, L. Chen and Y.-S. Hu, *Science*, 2020, **370**, 708–711.
3 M. Lee, J. Hong, J. Lopez, Y. Sun, D. Feng, K. Lim, W. C. Chueh, M. F. Toney, Y. Cui and Z. Bao, *Nat. Energy*, 2017, **2**, 861–868.
4 L. Su, Q. Xu, Y. Song, H. Wu, H. Chen, C. Shen and L. Wang, *Chem. Eng. J.*, 2022, **450**, 137978.
5 C. Delmas, *Adv. Energy Mater.*, 2018, **8**, 1703137.
6 N. Yabuuchi, K. Kubota, M. Dahbi and S. Komaba, *Chem. Rev.*, 2014, **114**, 11636–11682.
7 J.-Y. Hwang, S.-T. Myung and Y.-K. Sun, *Chem. Soc. Rev.*, 2017, **46**, 3529–3614.
8 Z. Li, Y. Zhang, J. Zhang, Y. Cao, J. Chen, H. Liu and Y. Wang, *Angew. Chem., Int. Ed.*, 2022, **61**, e202116930.
9 Y. Jin, P. M. L. Le, P. Gao, Y. Xu, B. Xiao, M. H. Engelhard, X. Cao, T. D. Vo, J. Hu, L. Zhong, B. E. Matthews, R. Yi, C. Wang, X. Li, J. Liu and J.-G. Zhang, *Nat. Energy*, 2022, **7**, 718–725.
10 F. Yang, F. Yu, Z. Zhang, K. Zhang, Y. Lai and J. Li, *Chemistry*, 2016, **22**, 2333–2338.
11 B. Li, B. Xi, Z. Feng, Y. Lin, J. Liu, J. Feng, Y. Qian and S. Xiong, *Adv. Mater.*, 2018, **30**, 1705788.
12 J. Liu, P. Kopold, C. Wu, P. A. van Aken, J. Maier and Y. Yu, *Energy Environ. Sci.*, 2015, **8**, 3531–3538.
13 Z. Tang, R. Zhang, H. Wang, S. Zhou, Z. Pan, Y. Huang, D. Sun, Y. Tang, X. Ji, K. Amine and M. Shao, *Nat. Commun.*, 2023, **14**, 6024.
14 Q. Meng, Y. Lu, F. Ding, Q. Zhang, L. Chen and Y.-S. Hu, *ACS Energy Lett.*, 2019, **4**, 2608–2612.
15 G. Wang, M. Shao, H. Ding, Y. Qi, J. Lian, S. Li, J. Qiu, H. Li and F. Huo, *Angew. Chem., Int. Ed.*, 2019, **58**, 13584–13589.
16 Y. Lu, N. Zhang, S. Jiang, Y. Zhang, M. Zhou, Z. Tao, L. A. Archer and J. Chen, *Nano Lett.*, 2017, **17**, 3668–3674.
17 J. Lin, L. Yao, C. Zhang, H. Ding, Y. Wu, S. Li, J. Han, G. Yue and D. Peng, *ACS Sustainable Chem. Eng.*, 2021, **9**, 11280–11289.
18 J. Ru, T. He, B. Chen, Y. Feng, L. Zu, Z. Wang, Q. Zhang, T. Hao, R. Meng, R. Che, C. Zhang and J. Yang, *Angew. Chem., Int. Ed.*, 2020, **59**, 14621–14627.
19 M. Liu, P. Zhang, Z. Qu, Y. Yan, C. Lai, T. Liu and S. Zhang, *Nat. Commun.*, 2019, **10**, 3917.
20 D. Y. W. Yu, P. V. Prikhodchenko, C. W. Mason, S. K. Batabyal, J. Gun, S. Sladkevich, A. G. Medvedev and O. Lev, *Nat. Commun.*, 2013, **4**, 2922.
21 F. Yang, W. Zhong, H. Wang, M. Ren, W. Liu, M. Li and L. Su, *J. Alloys Compd.*, 2020, **834**, 155204.
22 J. Zhou, X. Liu, L. Zhu, S. Niu, J. Cai, X. Zheng, J. Ye, Y. Lin, L. Zheng, Z. Zhu, D. Sun, Z. Lu, Y. Zang, Y. Wu, J. Xiao, Q. Liu, Y. Zhu, G. Wang and Y. Qian, *Chem*, 2020, **6**, 221–233.
23 Y. Liu, Q. Liu, C. Jian, D. Cui, M. Chen, Z. Li, T. Li, T. Nilges, K. He, Z. Jia and C. Zhou, *Nat. Commun.*, 2020, **11**, 2520.
24 H. Jin, S. Xin, C. Chuang, W. Li, H. Wang, J. Zhu, H. Xie, T. Zhang, Y. Wan, Z. Qi, W. Yan, Y.-R. Lu, T.-S. Chan, X. Wu, J. B. Goodenough, H. Ji and X. Duan, *Science*, 2020, **370**, 192–197.
25 Y. Sun, L. Wang, Y. Li, Y. Li, H. R. Lee, A. Pei, X. He and Y. Cui, *Joule*, 2019, **3**, 1080–1093.
26 Y. Liu, B. Zhou, S. Liu, Q. Ma and W.-H. Zhang, *ACS Nano*, 2019, **13**, 5885–5892.
27 K. Yang, J. Tang, Y. Liu, M. Kong, B. Zhou, Y. Shang and W.-H. Zhang, *ACS Nano*, 2020, **14**, 5728–5737.
28 Y. Liu, Y. Qing, B. Zhou, L. Wang, B. Pu, X. Zhou, Y. Wang, M. Zhang, J. Bai, Q. Tang and W. Yang, *ACS Nano*, 2023, **17**, 2431–2439.
29 D. Su, S. Dou and G. Wang, *Nano Energy*, 2015, **12**, 88–95.

30 H. Tan, D. Chen, X. Rui and Y. Yu, *Adv. Funct. Mater.*, 2019, **29**, 1808745.
31 S. Liu, Z. Luo, J. Guo, A. Pan, Z. Cai and S. Liang, *Electrochem. Commun.*, 2017, **81**, 10–13.
32 J. Huang, X. Guo, X. Du, X. Lin, J.-Q. Huang, H. Tan, Y. Zhu and B. Zhang, *Energy Environ. Sci.*, 2019, **12**, 1550–1557.
33 H. Shen, Y. An, Q. Man, D. Liu, X. Zhang, Z. Ni, Y. Dai, M. Dong, S. Xiong and J. Feng, *Adv. Funct. Mater.*, 2023, **34**, 2309834.
34 Y. Zhu, Q. Yao, R. Shao, C. Wang, W. Yan, J. Ma, D. Liu, J. Yang and Y. Qian, *Nano Lett.*, 2022, **22**, 7976–7983.
35 X. Li, X. Zhang, X. Niu, J. Zhang, R. Wu, J. S. Chen and Y. Yu, *Adv. Funct. Mater.*, 2023, **33**, 2300914.
36 H. Wu, L. Zheng, W. Liu, X. Xia, C. Xiao, J. Xie, L. Su, L. Wang and N. Du, *J. Alloys Compd.*, 2019, **771**, 169–175.
37 Y. Li, X. Zhong, X. Wu, M. Li, W. Zhang and D. Wang, *J. Mater. Chem. A*, 2021, **9**, 22364–22372.
38 H. Long, X. Yin, X. Wang, Y. Zhao and L. Yan, *J. Energy Chem.*, 2022, **67**, 787–796.
39 J. Sottmann, M. Herrmann, P. Vajeeston, Y. Hu, A. Ruud, C. Drathen, H. Emerich, H. Fjellvåg and D. S. Wragg, *Chem. Mater.*, 2016, **28**, 2750–2756.
40 Y. Tian, H. Li, S. Zhang, H. Zhang, G. Li, D. Liu, Y. Qi, Z. Jian, X. Cai, F. Li and W. Chen, *Energy Environ. Mater.*, 2020, **4**, 421–427.
41 X. X. Wang, Y. Wu, P. Huang, P. Chen, Z. Y. Wang, X. W. Xu, J. Xie, J. Yan, S. G. Li, J. Tu and Y. L. Ding, *Nanoscale*, 2020, **12**, 23682–23693.
42 Y.-H. Kim, J.-H. An, S.-Y. Kim, X. Li, E.-J. Song, J.-H. Park, K. Y. Chung, Y.-S. Choi, D. O. Scanlon, H.-J. Ahn and J.-C. Lee, *Adv. Mater.*, 2022, **34**, 2201446.
43 M. A. Ud Din, C. Li, L. Zhang, C. Han and B. Li, *Mater. Today Phys.*, 2021, **21**, 100486.
44 M. Wu, B. Xu, Y. Zhang, S. Qi, W. Ni, J. Hu and J. Ma, *Chem. Eng. J.*, 2020, **381**, 122558.
45 L. Wang, A. A. Voskanyan, K. Y. Chan, B. Qin and F. Li, *ACS Appl. Energy Mater.*, 2019, **3**, 565–572.
46 B. Pu, Y. Liu, J. Bai, X. Chu, X. Zhou, Y. Qing, Y. Wang, M. Zhang, Q. Ma, Z. Xu, B. Zhou and W. Yang, *ACS Nano*, 2022, **16**, 18746–18756.
47 J. Zhou, J. Chen, M. Chen, J. Wang, X. Liu, B. Wei, Z. Wang, J. Li, L. Gu, Q. Zhang, H. Wang and L. Guo, *Adv. Mater.*, 2019, **31**, 1807874.
48 C. C. Mayorga-Martinez, R. Gusmão, Z. Sofer and M. Pumera, *Angew. Chem., Int. Ed.*, 2018, **58**, 134–138.
49 Y. Huang, C. Zhu, S. Zhang, X. Hu, K. Zhang, W. Zhou, S. Guo, F. Xu and H. Zeng, *Nano Lett.*, 2019, **19**, 1118–1123.
50 X. Liu, S. Zhang, S. Guo, B. Cai, S. A. Yang, F. Shan, M. Pumera and H. Zeng, *Chem. Soc. Rev.*, 2020, **49**, 263–285.
51 L. B. Wang, C. C. Wang, F. J. Li, F. Y. Cheng and J. Chen, *Chem. Commun.*, 2018, **54**, 38–41.
52 H. Gao, J. Niu, C. Zhang, Z. Peng and Z. Zhang, *ACS Nano*, 2018, **12**, 3568–3577.
53 S. Guo, H. Li, Y. Lu, Z. Liu and X. Hu, *Energy Storage Mater.*, 2020, **27**, 270–278.
54 Y. Zhu, C. Wang, Z. Cheng, Q. Yao, J. Su, B. Chen, J. Yang and Y. Qian, *Chem. Commun.*, 2022, **58**, 5140–5143.
55 H. Gao, L. Song, J. Niu, C. Zhang, T. Kou, Y. Sun, J. Qin, Z. Peng and Z. Zhang, *J. Mater. Chem. A*, 2019, **7**, 13602–13613.
56 G. Liu, Z. Sun, X. Shi, X. Wang, L. Shao, Y. Liang, X. Lu, J. Liu and Z. Guo, *Adv. Mater.*, 2023, **35**, 2305551.
57 P. Xiong, P. Bai, A. Li, B. Li, M. Cheng, Y. Chen, S. Huang, Q. Jiang, X. H. Bu and Y. Xu, *Adv. Mater.*, 2019, **31**, 1904771.
58 H. Zhu, F. Wang, L. Peng, T. Qin, F. Kang and C. Yang, *Angew. Chem., Int. Ed.*, 2022, **62**, e202212439.
59 Y. Zhang, Q. Su, W. Xu, G. Cao, Y. Wang, A. Pan and S. Liang, *Adv. Sci.*, 2019, **6**, 1900162.
60 J. Chen, X. Fan, X. Ji, T. Gao, S. Hou, X. Zhou, L. Wang, F. Wang, C. Yang, L. Chen and C. Wang, *Energy Environ. Sci.*, 2018, **11**, 1218–1225.
61 H. Yang, L. W. Chen, F. X. He, J. Q. Zhang, Y. Z. Feng, L. K. Zhao, B. Wang, L. X. He, Q. B. Zhang and Y. Yu, *Nano Lett.*, 2020, **20**, 758–767.
62 H. Yang, R. Xu, Y. Yao, S. Ye, X. Zhou and Y. Yu, *Adv. Funct. Mater.*, 2019, **29**, 1809195.
63 P. Xue, N. Wang, Z. Fang, Z. Lu, X. Xu, L. Wang, Y. Du, X. Ren, Z. Bai, S. Dou and G. Yu, *Nano Lett.*, 2019, **19**, 1998–2004.
64 C. Wang, L. Wang, F. Li, F. Cheng and J. Chen, *Adv. Mater.*, 2017, **29**, 1702212.
65 J. Chen, X. Fan, Q. Li, H. Yang, M. R. Khoshi, Y. Xu, S. Hwang, L. Chen, X. Ji, C. Yang, H. He, C. Wang, E. Garfunkel, D. Su, O. Borodin and C. Wang, *Nat. Energy*, 2020, **5**, 386–397.
66 X. Zhang, X. Qiu, J. Lin, Z. Lin, S. Sun, J. Yin, H. N. Alshareef and W. Zhang, *Small*, 2023, **19**, 202302071.
67 L. Liang, Y. Xu, C. Wang, L. Wen, Y. Fang, Y. Mi, M. Zhou, H. Zhao and Y. Lei, *Energy Environ. Sci.*, 2015, **8**, 2954–2962.
68 J. Ni, X. Li, M. Sun, Y. Yuan, T. Liu, L. Li and J. Lu, *ACS Nano*, 2020, **14**, 9117–9124.
69 X. Li, M. Sun, J. Ni and L. Li, *Adv. Energy Mater.*, 2019, **9**, 1901096.
70 X. Li, S. Xiao, X. Niu, J. S. Chen and Y. Yu, *Adv. Funct. Mater.*, 2021, **31**, 2104798.
71 W. Xin, C. Lin, L. Fu, X.-Y. Kong, L. Yang, Y. Qian, C. Zhu, Q. Zhang, L. Jiang and L. Wen, *Matter*, 2021, **4**, 737–754.
72 K. Liu and L. Jiang, *Nano Today*, 2011, **6**, 155–175.
73 M.-Q. Zhao, H.-J. Peng, G.-L. Tian, Q. Zhang, J.-Q. Huang, X.-B. Cheng, C. Tang and F. Wei, *Adv. Mater.*, 2014, **26**, 7051–7058.
74 X. Zhang, X. Sun, S.-X. Guo, A. M. Bond and J. Zhang, *Energy Environ. Sci.*, 2019, **12**, 1334–1340.
75 T. A. Witten and L. M. Sander, *Phys. Rev. Lett.*, 1981, **47**, 1400–1403.
76 K. Fukami, S. Nakanishi, H. Yamasaki, T. Tada, K. Sonoda, N. Kamikawa, N. Tsuji, H. Sakaguchi and Y. Nakato, *J. Phys. Chem. C*, 2007, **111**, 1150–1160.
77 J. Chen, J. J. Davies, A. S. Goodfellow, S. M. D. Hall, H. G. Lancaster, X. Liu, C. J. Rhodes and W. Zhou, *Prog. Nat. Sci.*, 2021, **31**, 141–151.
78 U. Holzwarth and N. Gibson, *Nat. Nanotechnol.*, 2011, **6**, 534.
79 W. Li, D. Peng, W. Huang, X. Zhang, Z. Hou, W. Zhang, B. Lin and Z. Xing, *Carbon*, 2023, **204**, 315–324.

80 L. Cheng, C. Ma, W. Lu, X. Wang, H. Yue, D. Zhang and Z. Xing, *Chem. Eng. J.*, 2022, **433**, 133527.
81 Z. Li, W. Zhong, D. Cheng and H. Zhang, *J. Mater. Sci.*, 2021, **56**, 11000–11010.
82 X. Cheng, R. Shao, D. Li, H. Yang, Y. Wu, B. Wang, C. Sun, Y. Jiang, Q. Zhang and Y. Yu, *Adv. Funct. Mater.*, 2021, **31**, 2011264.
83 L. D. Ellis, B. N. Wilkes, T. D. Hatchard and M. N. Obrovac, *J. Electrochem. Soc.*, 2014, **161**, A416–A421.
84 H. Gao, W. Ma, W. Yang, J. Wang, J. Niu, F. Luo, Z. Peng and Z. Zhang, *J. Power Sources*, 2018, **379**, 1–9.
85 L. Chen, X. He, H. Chen, S. Huang and M. Wei, *J. Mater. Chem. A*, 2021, **9**, 22048–22055.
86 X. L. Cheng, D. J. Li, Y. Wu, R. Xu and Y. Yu, *J. Mater. Chem. A*, 2019, **7**, 4913–4921.
87 C. J. Hu, Y. S. Zhu, G. Y. Ma, F. Tian, Y. L. Zhou, J. Yang and Y. T. Qian, *Electrochim. Acta*, 2021, **365**, 137379.
88 S. Wei, W. Li, Z. Ma, X. Deng, Y. Li and X. Wang, *Small*, 2023, **19**, 2304265.
89 X. Xu, D. Chao, B. Chen, P. Liang, H. Li, F. Xie, K. Davey and S. Z. Qiao, *Angew. Chem., Int. Ed.*, 2020, **59**, 21728–21735.